Predictive Control of Photovoltaic Grid Connected Cascaded H-Bridge Converters During Unbalanced Voltage Sags

R.P Russelin
(P.G Student)M.E (P.E.D)
Narayanaguru College of Engineering,
Tamil Nadu,India
russelinreya1234@gmail.com

J.Evangelin Jeba
Assistant Professor B.E,M.E
Narayanaguru College of Engineering,
Tamil Nadu,India
eva.jaba@gmail.com

S.V Dishore
Assistant Professor B.Tech,M.Tech,(Ph.D)
Narayanaguru College of Engineering
Tamil Nadu,India
dishore312@gmail.com

***Abstract*—Multilevel cascade H-bridge (CHB) converters are one of the promising solutions for medium- and large-scale grid-connected photovoltaic power plants. However, there is a lack of a complete study about their operation during voltage sags. This paper proposes a flexible control strategy for the operation of photovoltaic grid-connected CHB inverters during unbalanced voltage sags. The key novelty is that the proposed strategy is able to inject both active and reactive powers to the grid with either balanced or unbalanced currents, while ensuring that all dc-link capacitor voltages remain balanced. The simulation and experimental evaluations of a 9-kVA grid-connected seven-level CHB illustrate and validate the performance of the proposed strategy for the operation of the grid-connected CHB converter during different unbalanced voltage sags.**

***Index Terms*—Photovoltaic systems, multilevel converter, cascaded H-bridge (CHB) converter, low-voltage ride-through (LVRT), active/reactive power injection, unbalanced voltage sag.**

I. Introduction

MULTILEVEL converters are a promising solution for medium- and large-scale grid-connected photovoltaic power plants (GCPVPPs), because of their ability to produce high-quality output voltage and current waveforms at medium/high-voltage ranges, while they require lower voltage rated power semiconductors and dc capacitors. Among various multilevel converter topologies, the multilevel cascaded H-bridge (CHB) converter, shown in Fig. 1, was introduced as a potential candidate for medium- and large-scale GCPVPPs in [1]–[8], because:

- The low switching frequency of each H-bridge semiconductor results in reduction of semiconductor losses.
- The total power losses of the GCPVPP with CHB converter are smaller than those from other topologies [9].
- Direct connection to medium-voltage grids eliminates the need for bulky and expensive line-frequency transformers.
- Multiple dc-links enable independent maximum power point tracking (MPPT) of the PV strings that maximizes the total extracted power.

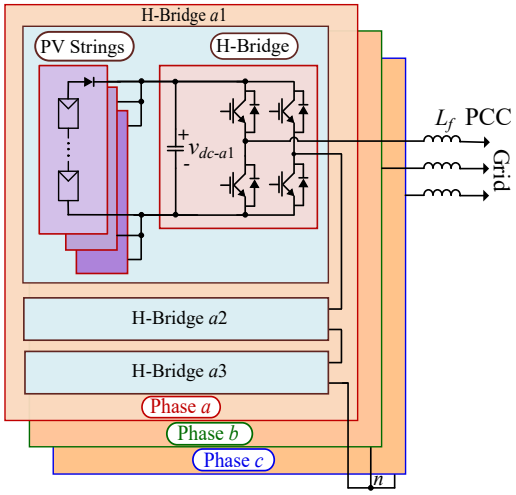

Fig. 1. Circuit configuration of the grid-connected photovoltaic power plant with 7L-CHB converter.

The performance of the proposed control strat-egy during a deep unbalanced voltage sag with reactive power injection and balanced currents is examined in this test, considering an unbalanced three-phase 70%

A grid-connected PV CHB inverter may experience inter-phase imbalance, which occurs when each phase generates a different amount of power as a result of the unbalanced phase currents or partial shading; and an additional inter-bridge imbalance which happens when each bridge in the same phase leg generates a different amount of power as a consequence of unequal power generation from the PV strings [4], [6]. These imbalances result in several issues: a) The output voltage quality of the converter deteriorates, b) the voltage of one dc-link may increase beyond its normal range, which can activate the dc-link over-voltage protection relay, which disconnects the converter from grid, and c) in the single-stage power conversion topology (without dc-dc converters), the deviation of dc-link voltages from their average value (V_{dc}), which is set to the voltage of PV strings maximum

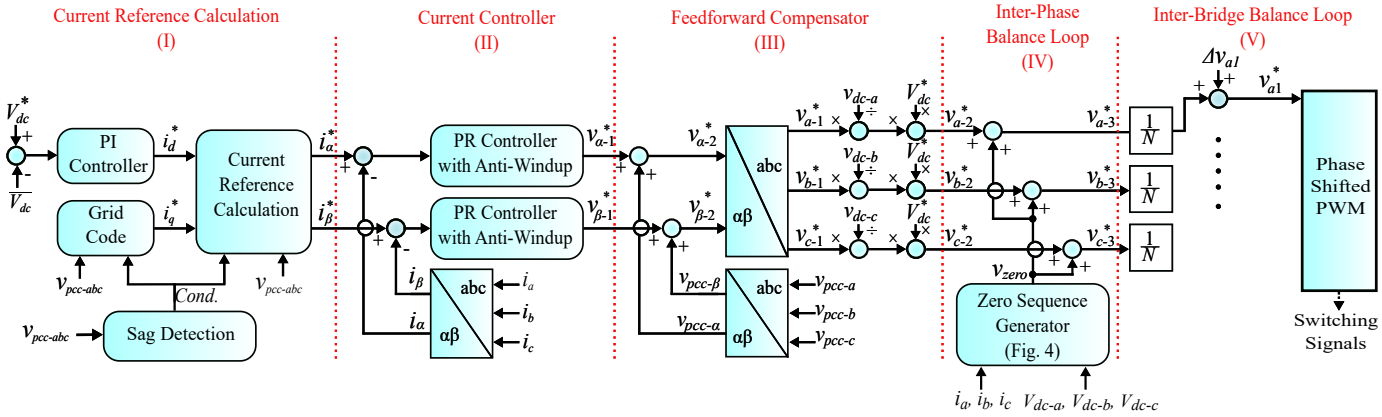

Fig. 2. Proposed control strategy for grid-connected CHB inverter during voltage sags.

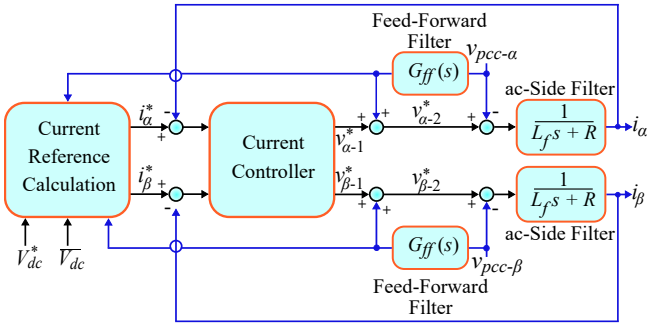

Fig. 3. Overview of control structure of the grid-connected photovoltaic power plant in $\alpha\beta$-frame.

power point (v_{mpp}), decreases the extracted power from PV strings [10].

With respect to the above mentioned issues, several algorithms are introduced in the literature to provide balanced current injection to the grid under different conditions. Various zero-sequence voltage injection algorithms are proposed in [4], [6], [7] to provide balanced current injection to the grid under dc-side imbalances, including partial shading or mismatch between PV strings. The balanced current injection under the failure of some of the bridges of the CHB inverter is addressed in [2]. The main goal of these studies is the zero-sequence voltage injection for achieving inter-phase balancing and injecting active power (p) with balanced currents to the grid during grid normal operation. A new GCPVPP topology with part-row and full-row connection of dc-dc converters to the CHB inverter is proposed in [5], which reduces the second harmonic oscillation of the dc-link voltage and provides balanced current injection during partial shading. An inter-bridge balancing through the modification of bridge voltage references is also presented in [7]. The operation of the CHB inverter during grid normal operation with balanced voltages and active power injection is addressed in these studies.

During unbalanced voltage sags, a grid-connected PV CHB inverter experiences inter-phase imbalance as a result of unbalanced phase currents; further inter-phase and inter-bridge imbalance can simultaneously occur as a result of unequal power generation from the PV strings (depending on irradiance conditions). Accordingly, various strategies are presented in [11]–[13], which achieve low-voltage ride-through capability for the CHB-based static synchronous compensator (STATCOM). Moreover, zero-sequence and negative-sequence current injection of the CHB-based STATCOM during grid disturbances are also taken into consideration in [14], [15]. The main disadvantage is that only reactive power injection is implemented on the grid-connected inverter in these studies, however, modern grid codes also require simultaneous active power injection with either balanced or unbalanced currents from grid-connected PV inverters [16], [17]. On top of that, a deep consideration with respect to the inter-phase and inter-bridge balancing is required. Therefore there is a need for a flexible control strategy, which can ensure dc-link voltage balancing, for the grid-connected PV CHB inverter during voltage sags, however, it is not investigated in the literature [1]–[7], [10]–[15].

Motivated by the above, this paper introduces a flexible control strategy for the operation of grid-connected PV CHB inverter during unbalanced voltage sags. The proposed strategy is capable of balancing dc-link voltages while injecting both active and reactive powers with either balanced or unbalanced currents. A zero-sequence voltage injection algorithm is proposed for inter-phase balancing, which allows for energy exchange between various phases. For inter-bridge balancing, the extracted power from different bridges of one phase is changed by modifying bridge voltage references. A feedforward voltage compensation is also applied to decrease the inverter transient current at the beginning of the voltage sag. The performance of the proposed control strategy is evaluated on the 9-kVA grid-connected 7L-CHB inverter simulation and experimental setups under various voltage sags, to validate the capability of the proposed algorithm for the operation of the grid-connected CHB inverter during voltage sags. Unbalanced voltage sags are more common compared to balanced voltage sags and the operation of the grid-connected PV CHB inverter during balanced voltage sags or normal grid condition is also easier to deal with. Therefore, unbalanced voltage sags are taken into consideration in all of the investigated case studies in this paper, while the proposed control strategy can also be used during grid normal operation or balanced voltage sags. Notice

that for those operations, MPPT can always be implemented, however it is not a mandatory objective of this manuscript.

The rest of the paper is organized as follows. Section II provides an overview of the proposed strategy for grid-connected CHB inverter during voltage sags, including detailed discussions about the proposed feedforward compensator and inter-phase and inter-bridge controllers. The simulation and experimental results are presented in Sections III and IV, respectively, while the conclusions of the work are summarized in Section V.

II. Proposed Control Strategy for Grid-Connected PV CHB Inverter

The circuit configuration of the GCPVPP with 7L-CHB converter is illustrated in Fig. 1. A detailed description of the GCPVPP with grid-connected CHB inverter can be found in [4], [6]. In order to generalize the proposed strategy, an N-level CHB is considered in this section. The structure of the proposed control strategy, divided into five different parts, is depicted in Fig. 2. These parts will be described in detail in the following subsections.

A simplified overview of the control structure of the GCPVPP with CHB inverter in the $\alpha\beta$-frame is presented in Fig. 3. The grid voltages ($v_{pcc\text{-}\alpha}$ and $v_{pcc\text{-}\beta}$) are fed into the current reference calculation algorithm to determine the reactive current reference according to the grid-codes, while the dc-link voltages are also applied to calculate the active current reference. The current controller, which is implemented in the $\alpha\beta$-frame, calculates the voltage references based on the error between current references (i_α^* and i_β^*) and instantaneous grid currents (i_α and i_β). The feed-forward filtered voltages from the grid are added to the calculated voltage reference from the current controller to generate the output voltage of the converter. Finally, the ac-side filter model is implemented to determine the grid currents, which are used as feedback in the controller. The details of the model of the ac-side filter can be found in [18].

The controller of the CHB inverter is used to maintain the average dc-link voltage ($\overline{V_{dc}}$) by controlling the injected active power into the grid. $\overline{V_{dc}}$ is calculated as follows:

$$\overline{V_{dc}} \triangleq \frac{\sum_{x=a}^{c}\sum_{j=1}^{N} v_{dc-xj}}{N \times 3}, \tag{1}$$

where $x \in \{a,\ b,\ c\}$. The bridge number is denoted by j, while v_{dc-xj} is the dc-link voltage of bridge xj. As illustrated in Fig. 2, the error between $\overline{V_{dc}}$ and V_{dc}^*, which is the bridge voltage reference, is fed into a PI controller, that calculates the d-axis current reference (i_d^*). In this study, a sag detection second-order generalized integrator (SOGI) based orthogonal system is applied for the calculation of the amplitude of phase voltages and determination of the minimum phase voltage amplitude. The detailed description on the SOGI implementation and voltage sag detection can be found in [16]. Based on the amplitude of the voltage sag, the q-axis current reference (i_q^*) is calculated from grid codes, as implemented in [15].

In order to show the flexibility of the proposed strategy, two different current reference calculation strategies are demonstrated in this study: 1) Balanced currents during balanced/unbalanced voltage sags, as in [19], which uses the full current capacity of the inverter to enhance the point of common coupling (PCC) during voltage sags, and 2) unbalanced currents during unbalanced voltage sags in order to achieve zero active power oscillation, as in [20].

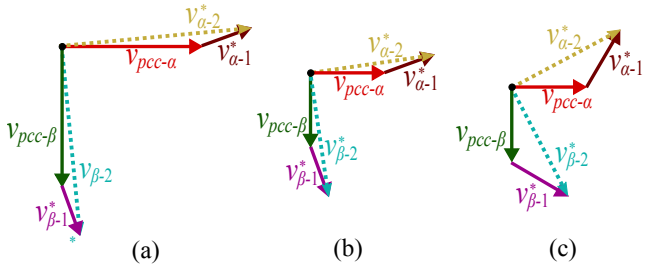

Fig. 4. Feedforward voltage compensation principle - voltage references: (a) During the grid normal operation, (b) at the beginning of the voltage sag and (c) during the steady-state period of the voltage sag.

The errors between the calculated current references and instantaneous phase currents, transformed to the $\alpha\beta$ coordinate (i_α and i_β), are fed into the proportional resonant (PR) with anti-windup controllers. Although the implementation of the conventional PI controller for balanced current injection is simpler, it requires multiple frame transformations and results in reduced dynamic performance as compared with abc-framework-based controllers [21]–[23]. The anti-windup control loop prevents the saturation of the output voltage of the PR controller and maintains the sinusoidal shape of the output voltage reference. Furthermore, for injection of accurate unbalanced currents under unbalanced voltage sags, the calculation of both positive- and negative-sequence voltages in dq frame is required, which increases the computational complexity [22]. Furthermore, the PR controller with anti-windup shows faster dynamic response and zero steady-state error [24]. The voltage references ($v_{\alpha\text{-}1}^*$ and $v_{\beta\text{-}1}^*$) are calculated through PR controllers. Subsequently feedforward compensator and voltage balancing controllers are implemented and their detailed descriptions are provided in the following subsections. Finally, the conventional phase-shifted pulse-width modulation algorithm is implemented to generate the switching signals. The detailed explanation of this algorithm can be found in [25], [26].

A. Effects of Feedforward Voltage Compensation

Fast detection of voltage sags is important for quick operation of the controller [27]. A maximum delay of $T/4$, where T is the grid voltage period, is introduced by the SOGI due to the single-phase quadrature signal generation. It should be noted that this delay also depends on the amplitude of the voltage sag.

The delay of the voltage sag detection algorithm, leads to a high transient current at the beginning of voltage sags because the controller continues to inject maximum power to the grid in the period between the occurrence of the voltage sag and its detection. Thus, the use of a feedforward voltage compensator is necessary to decrease the transient current during this

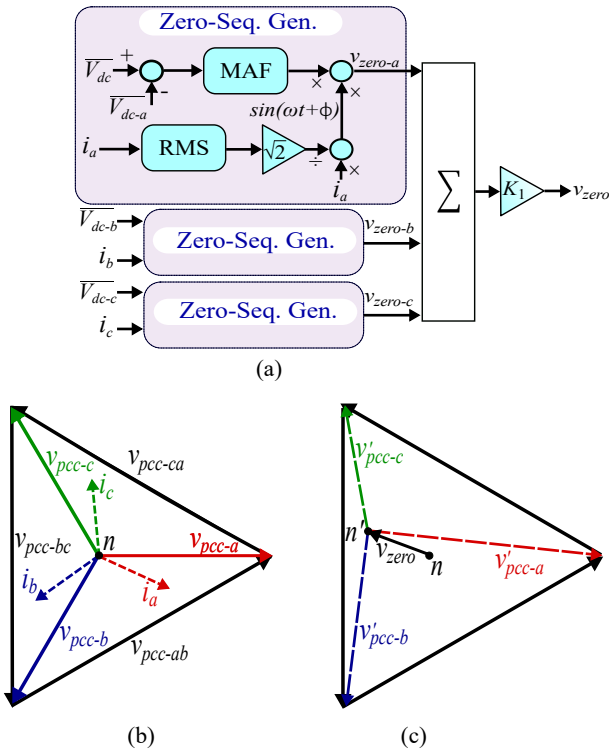

Fig. 5. Proposed inter-phase balancing algorithm: (a) Proposed zero-sequence generation strategy, (b) vector diagram during balanced operation and (c) vector diagram during zero-sequence voltage injection.

period. A feedforward voltage compensator is implemented based on [24], as depicted in Fig. 2. The instantaneous PCC voltages ($v_{pcc\text{-}\alpha}$ and $v_{pcc\text{-}\beta}$), which are transformed to $\alpha\beta$ coordinate using the Clark transformation, are added to $v^*_{\alpha\text{-}1}$ and $v^*_{\beta\text{-}1}$, respectively, as follows:

$$\begin{aligned} v^*_{\alpha\text{-}2} &= v^*_{\alpha\text{-}1} + v_{pcc\text{-}\alpha}, \\ v^*_{\beta\text{-}2} &= v^*_{\beta\text{-}1} + v_{pcc\text{-}\beta}. \end{aligned} \tag{2}$$

The vector diagram during the grid normal operation is depicted in Fig. 4(a). During such condition, the inverter operates under unity power factor and the output voltage of the inverter has a similar phase and amplitude as v_{pcc}. Accordingly, a large portion of $v^*_{\alpha\text{-}2}$ and $v^*_{\beta\text{-}2}$ are provided by $v_{pcc\text{-}\alpha}$ and $v_{pcc\text{-}\beta}$, respectively, while the current controller only regulates the required voltage drop on the filter inductors for the intended current references. Therefore, the amplitudes of $v^*_{\alpha\text{-}1}$ and $v^*_{\beta\text{-}1}$ are small during the grid normal operation.

At the beginning of the voltage sag, as shown in Fig. 4(b), the instantaneous values of $v_{pcc\text{-}\alpha}$ and $v_{pcc\text{-}\beta}$ are reduced immediately, following the voltage sag amplitude. At the same time, the values of $v^*_{\alpha\text{-}1}$ and $v^*_{\beta\text{-}1}$ cannot change immediately, because they depend on the voltage sag detection algorithm, current reference calculation method and current controller. Consequently, $v^*_{\alpha\text{-}2}$ and $v^*_{\beta\text{-}2}$ decrease instantaneously at the beginning of the voltage sag. This reduces the output voltage of the inverter at the beginning of the voltage sag and decreases its transient current. It should be noted that without this feedforward compensator, the voltage references are only regulated through the current controller, which cannot react

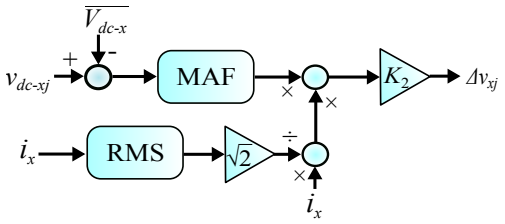

Fig. 6. Inter-bridge balancing algorithm.

instantaneously to the voltage sag and hence the transient current becomes large at the beginning of the voltage sag. Finally, a feed-forward voltage controller for reducing the effect of the variation of dc-link voltage is also implemented by multiplying the voltage references by $V^*_{dc}/v_{dc\text{-}xj}$.

B. Proposed Inter-Phase Balancing Strategy

An inter-phase balancing strategy is implemented by adding a zero-sequence voltage (v_{zero}) to the voltage references ($v^*_{a\text{-}2}$, $v^*_{c\text{-}2}$ and $v^*_{c\text{-}2}$), as shown in Part IV of Fig. 2.

The proposed algorithm for the calculation of v_{zero} is presented in Fig. 5(a). The error between $\overline{V_{dc}}$ and the average of the bridge voltages of phase a ($\overline{V_{dc\text{-}a}} = (v_{dc\text{-}a1} + v_{dc\text{-}a2} + ... + v_{dc\text{-}aN})/N$) is fed into a moving average filter (MAF), which filters instantaneous oscillations of the dc-link voltages by performing the following operation:

$$\overline{x}(t) = \frac{1}{T_w}\int_{t-T_w}^{t} x(\tau)d\tau, \tag{3}$$

where T_w is the window width of the MAF and $\overline{x}(t)$ is the moving average value of $x(t)$ calculated over T_w. A window width of $T_w = 1/(2f)$, where f is the grid frequency, can remove all the second-order oscillations of the dc-link voltages. The proposed inter-phase voltage balancing algorithm is designed to balance the average dc component of the capacitor voltages with a bandwidth of 20 Hz. Therefore, the effect of delay of the MAF block ($1/(2f)$), with a bandwidth of 100 Hz, can be neglected on the performance of the proposed inter-phase voltage balancing algorithms [24], [28].

The calculated average error from the MAF is then multiplied by $sin(\omega t + \phi)$, while $i_a = I_m sin(\omega t + \phi)$. As shown in Fig. 5(a), the instantaneous value of $sin(\omega t + \phi)$ is approximated as:

$$sin(\omega t + \phi) \approx \frac{i_a}{RMS(i_a) \times \sqrt{2}}, \tag{4}$$

in which, $RMS(i_a)$ is the rms value of the current, calculated dynamically in the controller. Subsequently, the calculated zero-sequence voltage from phase a ($v_{zero\text{-}a}$) is added to $v_{zero\text{-}b}$ and $v_{zero\text{-}c}$. The total zero voltage (v_{zero}) is adjusted using a proportional controller with a proportional gain of K_1, which ensures the inter-phase balancing of the grid-connected CHB inverter during unbalanced voltage sags.

The vector diagram of the CHB inverter, during balanced operation, is depicted in Fig. 5(b). In this condition, the injected zero-sequence voltage is zero. The operation of the

proposed inter-phase balancing strategy is investigated considering $v_{dc\text{-}a} > \overline{V_{dc}}$ and $v_{dc\text{-}b},\ v_{dc\text{-}c} < \overline{V_{dc}}$. The corresponding voltages and currents vector diagram after the injection of the proposed zero-sequence voltage are presented in Fig. 5(c). Since $v_{dc\text{-}a} - \overline{v_{dc}} < 0$, $v_{zero\text{-}a}$ is in the opposite direction of i_a. Similarly, $v_{zero\text{-}b}$ and $v_{zero\text{-}c}$ are in the same direction of i_b and i_c, respectively. Thus, the neutral point of the CHB inverter is moved from n to n', by a vector of v_{zero}. The amplitude of the new voltage vector of phase a (v'_a) is larger than phases b and c (v'_b and v'_c). Therefore, the extracted power from phase a ($p'_a = v'_a.i_a$) is larger than p'_b and p'_c, which means that the extracted power from the capacitors of phase a is larger than b and c. As a consequence, $v_{dc\text{-}a}$ reduces and dc-link capacitors become balanced. It should be noted that because the proposed method of zero-sequence voltage injection depends on the current direction, it can achieve inter-phase balancing under all different types of current injection including active/reactive power injection with balanced/unbalanced currents.

C. Inter-Bridge Balancing Strategy

It is important that all of the dc-link voltages of each phase remain equal to achieve high-quality output voltages. Since the current of all of the bridges of one phase are equal, their voltage varies if their power is different. An inter-bridge balancing mechanism, shown in Part V of Fig. 2, is implemented in this study as in [7]. The voltage reference of each bridge is calculated by dividing the voltage reference of the phase ($v^*_{a\text{-}3}$) by N and subsequently, is added with Δv_{xj}, which is the required deviation of the voltage reference of each bridge for inter-bridge balancing. The proposed algorithm for the calculation of Δv_{xj} is presented in Fig. 6(a). The difference between $v_{dc\text{-}xj}$ and $\overline{V_{dc}}$ is fed into the MAF, as defined in (3). The filtered voltage difference is then multiplied by $sin(\omega t + \phi)$ (4) and fed into a proportional controller with a proportional gain of K_2 to calculate Δv_{xj}.

III. Simulation Results

The GCPVPP with 7L-CHB inverter (Fig. 1(a)) is modeled and developed using Matlab/Simulink© and PLECS toolbox. The main system parameters are listed in Table I. The aim of the paper is to analyze the performance of the proposed inter-phase and inter-bridge voltage balancing algorithms during grid voltage sags. Although the MPPT stage is not implemented, the dc-link voltage is still regulated by the current reference generation. This does not affect the purpose of this paper to demonstrate the control and operation of the CHB inverter [2], [4], [6], because: i) The extracted power from PV strings is close to the their maximum power by setting the dc-link voltages to the voltage of the maximum power. ii) The oscillation of the extracted power from PV strings, due to the oscillation of the dc-link voltage, is small compared to its average value. iii) During voltage sags, injection of reactive power to the grid is required by the grid codes. The extracted power from PV strings is reduced based on the amount of injected reactive current and the inverter nominal current.

Since three H-bridges are cascaded in each phase leg, the converter output phase voltages feature seven-level waveforms with an equivalent switching frequency of $3.6\,\mathrm{kHz}$. In order to evaluate the flexibility of the proposed strategy, two different voltage sag conditions are investigated: 30% single-phase voltage sag with simultaneous injection of active and reactive powers with unbalanced currents (*Case I*), and 70% unbalanced three-phase voltage sag with reactive power injection and balanced currents (*Case II*). The simulation results on a 9-kVA GCPVPP are presented in this paper. These case studies have also been tested on 10-MVA GCPVPP, connected to the $6.6\,\mathrm{kV}$ distribution network, and similar performances have been achieved.

TABLE I
Simulation and Experimental Parameters

Parameter	Symbol	Value
PV panel parameters		
PV string maximum power	p_{mpp}	$1\,\mathrm{kW}$
PV string *MPP* voltage	v_{mpp}	$145\,\mathrm{V}$
PV string *MPP* current	i_{mpp}	$7\,\mathrm{A}$
Number of series-connected PV panels in the PV string	N_s	5
Number of parallel-connected PV panels in the PV string	N_p	1
7L-CHB inverter parameters		
Apparent power	S	$9\,\mathrm{kVA}$ $(1\,\mathrm{pu})$
PCC voltage	$v_{pcc\text{-}ll}$	$430\,\mathrm{V_{rms}}$ $(1\,\mathrm{pu})$
Inductor filter	L_f	$8\,\mathrm{mH}$ $(0.15\ \mathrm{pu})$
dc-link voltage	v_{dc}	$145\,\mathrm{V}$
dc-link capacitor	$C_{dc\text{-}xj}$	$4.5\,\mathrm{mF}$
Carrier frequency	f_{carr}	$600\,\mathrm{Hz}$
Apparent switching frequency	f_{sw}	$3.6\,\mathrm{kHz}$
Control parameters		
PR current controller	k_{p1}, k_r	$0.003, 0.1$
Inter-phase/inter-bridge voltage balancing	k_1, k_2	$0.005, 0.005$
dc-link voltage controller	k_{p2}, k_i	$0.15, 0.6$
Feed-forward filter time-constant	τ	$0.00001\,\mathrm{s}$

Case I: This case demonstrates the operation of the CHB inverter during 30% single-phase voltage sag, which can occur as a result of a single-line to ground fault in the power system. This voltage sag requires simultaneous injection of active and reactive power, according to the grid codes [29]. The unbalanced current injection method is chosen in this case, which results in zero active power oscillation from the inverter. The voltage sag occurs at phase b with duration of $150\,\mathrm{ms}$. The three-phase grid voltages (v_{pcc}) and injected currents (i_{abc}) are depicted in Fig. 7(a). Before $t = 0.05\,\mathrm{ms}$, the grid is at normal condition and the inverter injects active power to the grid with balanced currents (Fig. 7(c)), while no phase-displacement exists between the phase currents and voltages. Since the minimum amplitude of the voltage sag in this test study is larger than $0.5\,\mathrm{pu}$, the inverter injects both active and reactive powers to the grid between $t = 0.05\,\mathrm{ms}$ and $t = 0.2\,\mathrm{ms}$. A second harmonic voltage oscillation exists in both active and reactive powers, due to the injection of balanced currents to the PCC with unbalanced voltages.

It can be seen from Fig. 7(b) that the transient current of the inverter at the beginning of the voltage sag is reduced through the feedforward voltage compensator. The current of phase b, the phase with the voltage sag, remains equal to the nominal current of the inverter ($11\,\mathrm{A_{rms}}$), while the currents

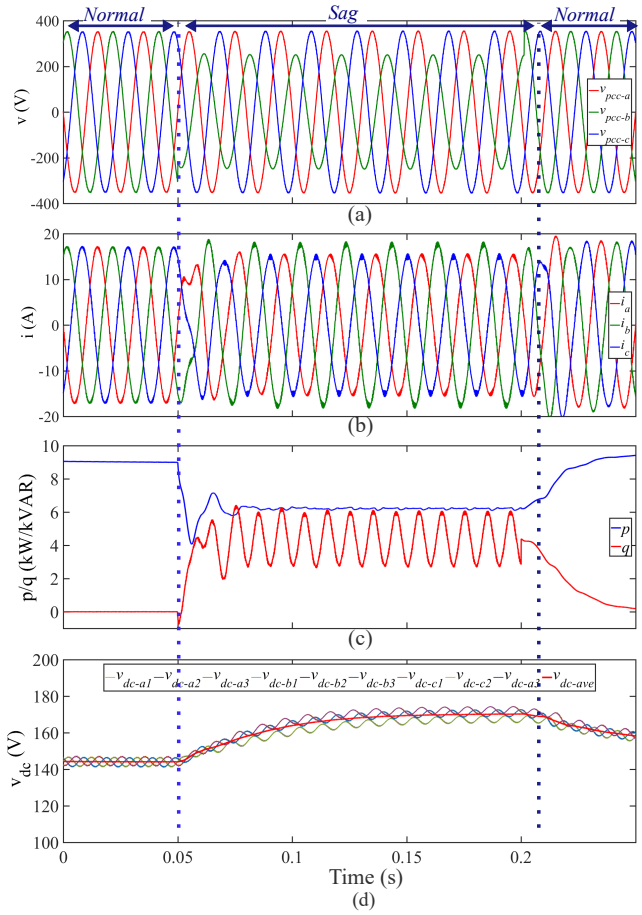

Fig. 7. Simulation results of 9-kVA grid-connected 7L-CHB inverter. *Case I* - 30% single-phase voltage sag with unbalanced current injection: (a) PCC voltages, (b) inverter output currents, (c) injected active/reactive power to the grid and (d) dc-link voltages.

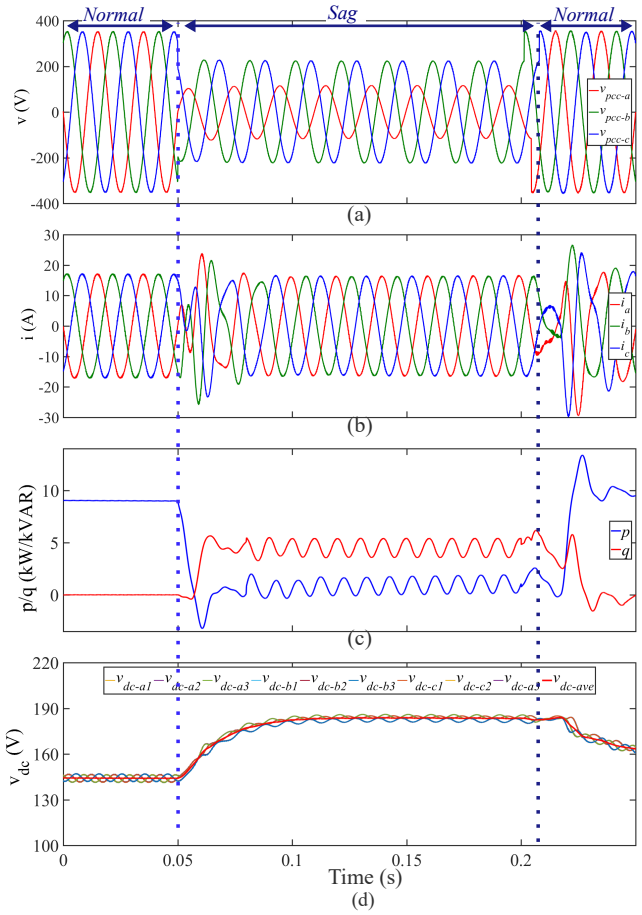

Fig. 8. Simulation results of 9-kVA grid-connected 7L-CHB inverter. *Case II* - 70% three-phase voltage sag with balanced current injection: (a) PCC voltages, (b) inverter output currents, (c) injected active/reactive power to the grid and (d) dc-link voltages.

of nonfaulty phases reduce to $9.2\,\mathrm{A_{rms}}$. The bridge capacitor voltages ($v_{dc\text{-}xj}$), presented in Fig. 7(d), are balanced and their average remains close to 165 V during this unbalanced voltage sag condition. The extracted powers from PV strings are decreased to 6 kW, due to the current limitation of the inverter as a consequence of reactive power injection during the voltage sag. After the clearance of the voltage sag, the output power of the inverter recovers to 9 kW and reactive power reduces to zero, while capacitor voltages stay balanced.

Case II: The performance of the proposed control strategy during a deep unbalanced voltage sag with reactive power injection and balanced currents is examined in this test, considering an unbalanced three-phase 70% voltage sag (phase a experiences deeper voltage sag compared to phases b and c), as shown in Fig. 8(a). The inverter injects 3.8 kVAR average reactive power to the grid, while the injected active power decreases to zero. The dc-link voltages remain balanced. The presented simulation results verify the flexibility of the proposed strategy under various voltage sags and different power/current injection strategies.

IV. Experimental Evaluation

Fig. 9(a) and (b) show the circuit diagram and the hardware setup, respectively, for a 9-kVA three-phase 7L-CHB converter. The parameters of the CHB prototype are listed in Table I. Due to safety issues and limited testing capabilities of the university laboratory, the experimental validation is performed on a scaled down GCPVPP. The grid interfacing inductor for the simulation is selected to have a close per unit value as the experimental setup. Therefore, these two systems are equivalent and show similar performances. The converter is fed by nine isolated Elgar TerraSAS PV simulators from Ametek, each of which was programmed to simulate the electrical behavior of a PV string, with a solar irradiance of $1000\,\mathrm{W/m^2}$ and a module temperature of 25°C. The control strategy is implemented on a dSPACE DS1006 platform with onboard Xilinx FPGA modules operating at 100 MHz. A programmable 20kVA AC power source, model TopCon TC.ACS 4 quadrant, with capability of simulating various voltage sag conditions is used as a grid. The proposed controller has been evaluated under three different voltage sag conditions and power and current injection strategies.

Case I: This case experimentally examines the performance of the proposed control strategy during a 30% single-

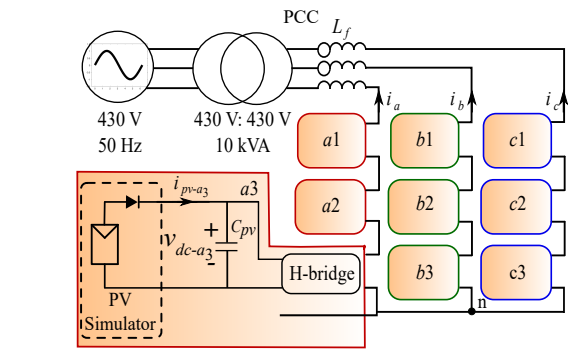

(a)

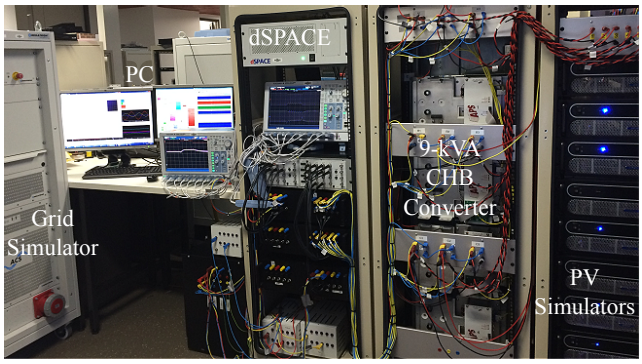

(b)

Fig. 9. Experimental verification: (a) Circuit diagram of the grid-connected CHB inverter test system and (b) setup of the experiment.

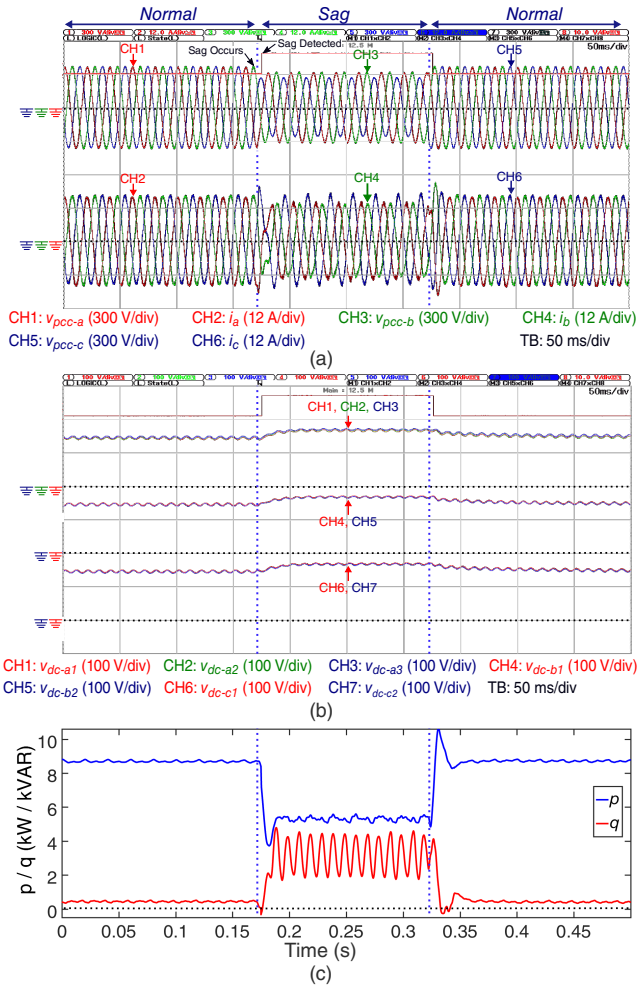

Fig. 10. Experimental results of grid-connected 7L-CHB inverter. *Case I* - 30% single-phase voltage sag with unbalanced current injection: (a) PCC voltages and currents, (b) dc-link voltages and (c) injected active/reactive power to the grid.

phase voltage sag, which requires simultaneous injection of active and reactive power to the grid. Unbalanced current injection is also taken into consideration. The sag occurs in phase c for a duration of $150\,\mathrm{ms}$. The three-phase grid voltages (v_{pcc}) and injected currents (i_{abc}) are depicted in Fig. 10(a). The delay between the beginning of the voltage sag and its detection is also presented in this figure. The transient currents during this time are not large, as a result of the proposed feedforward voltage compensator. The current of phase c, the phase with the voltage sag, remains equal to the nominal current of the inverter ($11\,\mathrm{A_{rms}}$), while the currents of nonfaulty phases reduce to $9.2\,\mathrm{A_{rms}}$. This leads to zero active power oscillation to the grid during such unbalanced voltage sag, as depicted in Fig. 10(c). The average active power reduces to $5.3\,\mathrm{kW}$, while the average reactive power increases to $3.1\,\mathrm{kVAR}$.

The bridge capacitor voltages are depicted in Fig. 10(b). Before $t = 0.175\,\mathrm{s}$, which grid is in normal operation mode, the capacitor voltages are balanced and their average voltage is equal to $145\,\mathrm{V_{dc}}$, which is equal to v_{mpp} of the simulated PV string. This results in the extraction of maximum power from all of the PV strings, which in total is equal to $9\,\mathrm{kW}$ as presented in Fig. 10(c). The implementation of the proposed inter-phase and inter-bridge balancing schemes leads to the balanced capacitor voltages during the voltage sag. The reduction of the power from PV strings during the voltage sag is performed by increasing the voltage of PV panels to $168\,\mathrm{V}$.

Case II: This case study demonstrates a three-phase 70% unbalanced voltage sag (phase a experiences deeper voltage sag compared to phases b and c) in order to verify the performance of the proposed control strategy during reactive power injection with balanced currents, and results are displayed in Fig. 11. A three-phase to ground fault can be the reason of such voltage sag at PCC. It can easily be seen that the transient current of the inverter at the beginning of such deep voltage sag is not large. During the voltage sag, the amplitude of currents remain as its nominal value, while a phase displacement of $\pi/2$ exists between the phase current and voltage. This indicates the injection of reactive power to the grid with an average value of $3.4\,\mathrm{kVAR}$, while the average injected active power is zero. A second harmonic oscillation exists in both active and reactive powers due to the injection of balanced currents to the PCC with unbalanced voltages. The dc-capacitor voltage are balanced during the voltage sag and their average is increased to $177\,\mathrm{V}$ (equal to the open-circuit voltage of the PV panel) in order to reduce the extracted power from the PV panels to zero.

Case III: The performance of the proposed controller in balancing the capacitor voltages under an unbalanced voltage sag with long duration is evaluated in this case study. The

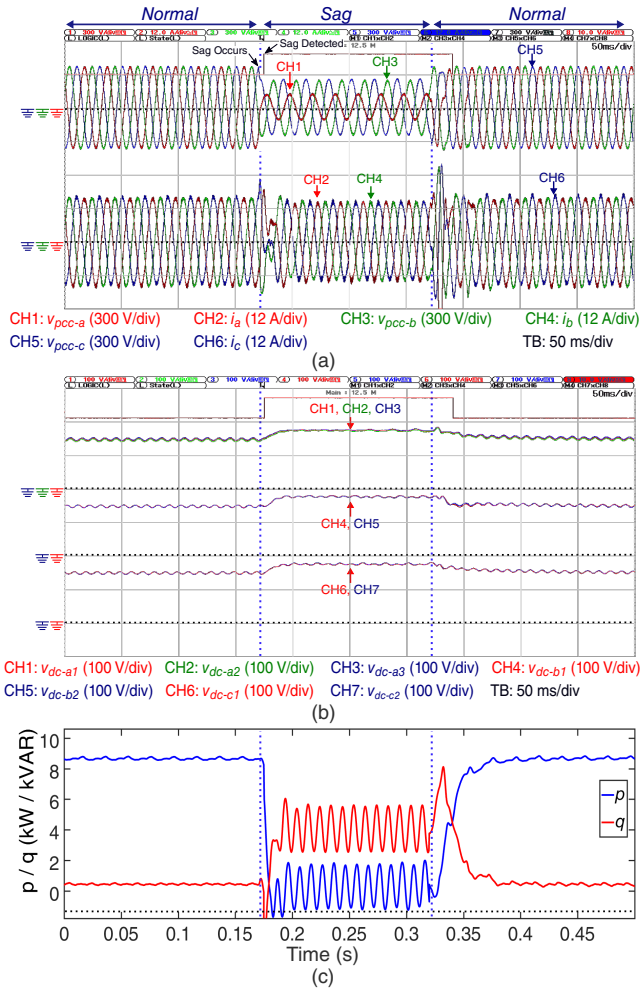

Fig. 11. Experimental results of grid-connected 7L-CHB inverter. *Case II* - 70% three-phase voltage sag with balanced current injection: (a) PCC voltages and currents, (b) dc-link voltages and (c) injected active/reactive power to the grid.

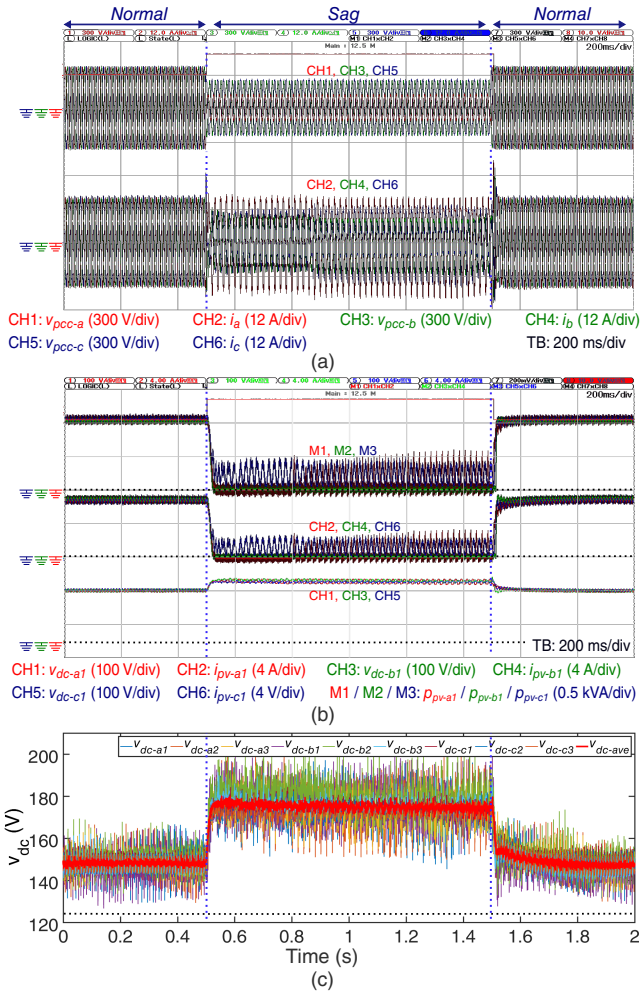

Fig. 12. Experimental results of grid-connected 7L-CHB inverter. *Case III* - 70% long-duration three-phase voltage sag with unbalanced current injection: (a) PCC voltages and currents, (b) PV panels voltages, powers and (c) dc-link voltages.

simulated voltage sag is similar to *Case II*, although its duration is increased to 1 s. Besides, the unbalanced current injection strategy is taken into consideration in order to verify the flexibility of the proposed strategy and results are depicted in Fig. 12. The extracted power and current from the PV modules decrease to zero during the voltage sag, as shown in Fig. 12(b). The dc-link voltage of all of the nine bridges and its average are depicted in Fig. 12(c). $\overline{V_{dc}}$ is equal to 145 V (v_{mpp}) during the grid normal operation, while it increases to 177 V during the voltage sag. It can be seen, the dc-link voltages remain balanced during such unbalanced voltage sag with a long duration, which shows the stable operation of CHB inverter during unbalanced voltage sags.

It can be seen that the proposed control algorithm is able to provide voltage balancing between all of the capacitors of the CHB converter during all operation conditions, including balanced or unbalanced current injection to the grid.

V. Conclusion

Active/reactive power injection is required for medium- and large- scale GCPVPPs during voltage sags, however, there is lack of a detailed study in the literature for the operation of grid-connected CHB inverters, which are a promising candidate for these types of GCPVPPs. Accordingly, a flexible control strategy for the operation of the photovoltaic grid-connected CHB inverter during unbalanced voltages sags has been introduced in this paper. A zero-sequence voltage injection has been introduced in order to achieve the inter-phase balancing, while the inter-bridge balancing has been obtained through the modification of bridges voltage references. Transient currents of the inverter, at the beginning of the voltage sag have been greatly reduced by implementing a feedforward voltage compensator.

Detailed implementation of the proposed control strategies has been presented, and its effectiveness has been demonstrated through simulation and experimental results on a 9-kVA GCPVPP, during different unbalanced voltage sag conditions. The CHB inverter is capable of achieving low-voltage ride-through and is able to inject the required amount of active and reactive power to the grid according to the grid codes. Flexibility of the proposed controller has also been verified under two different current injection strategies: a)

balanced current injection with the advantage of using the full current capacity of the inverter in enhancing the PCC voltage, and b) unbalanced current injection with zero active power oscillation. The evaluation results verify the applicability of the proposed control strategy for medium- and large-scale GCPVPPs during voltage sags.

REFERENCES

[1] C. D. Fuentes, C. A. Rojas, H. Renaudineau, S. Kouro, M. A. Perez, and M. Thierry, "Experimental validation of a single dc bus cascaded H-bridge multilevel inverter for multistring photovoltaic systems," *IEEE Trans. Ind. Electron.*, vol. 64, no. 2, pp. 930–934, Oct. 2016.

[2] Y. Yu, G. Konstantinou, B. Hredzak, and V. G. Agelidis, "Operation of cascaded H-bridge multilevel converters for large-scale photovoltaic power plants under bridge failures," *IEEE Trans. Ind. Electron.*, vol. 62, no. 11, pp. 7228–7236, Nov. 2015.

[3] P. Sochor and H. Akagi, "Theoretical comparison in energy-balancing capability between star- and delta-configured modular multilevel cascade inverters for utility-scale photovoltaic systems," *IEEE Trans. Power Electron.*, vol. 31, no. 3, pp. 1980–1992, Mar. 2016.

[4] Y. Yu, G. Konstantinou, B. Hredzak, and V. G. Agelidis, "Power balance optimization of cascaded H-bridge multilevel converters for large-scale photovoltaic integration," *IEEE Trans. Power Electron.*, vol. 31, no. 2, pp. 1108–1120, Feb. 2016.

[5] C. D. Townsend, Y. Yu, G. Konstantinou, and V. G. Agelidis, "Cascaded H-bridge multilevel PV topology for alleviation of per-phase power imbalances and reduction of second harmonic voltage ripple," *IEEE Trans. Power Electron.*, vol. 31, no. 8, pp. 5574–5586, Aug. 2016.

[6] Y. Yu, G. Konstantinou, B. Hredzak, and V. G. Agelidis, "Power balance of cascaded H-bridge multilevel converters for large-scale photovoltaic integration," *IEEE Trans. Power Electron.*, vol. 31, no. 1, pp. 292–303, Jan. 2016.

[7] H. Akagi, S. Inoue, and T. Yoshii, "Control and performance of a transformerless cascade PWM STATCOM with star configuration," *IEEE Trans. Ind. Appl.*, vol. 43, no. 4, pp. 1041–1049, Jul. 2007.

[8] Y. Yu, G. Konstantinou, C. D. Townsend, R. P. Aguilera, and V. G. Agelidis, "Delta-connected cascaded H-bridge multilevel converters for large-scale PV grid integration," *IEEE Trans. Ind. Electron.*, vol. 64, no. 11, pp. 8877–8886, Nov. 2017.

[9] J. Sastry, P. Bakas, H. Kim, L. Wang, and A. Marinopoulos, "Evaluation of cascaded H-bridge inverter for utility-scale photovoltaic systems," *Renewable Energy*, vol. 69, pp. 208 – 218, Sep. 2014.

[10] B. Xiao, L. Hang, J. Mei, C. Riley, L. M. Tolbert, and B. Ozpineci, "Modular cascaded H-bridge multilevel PV inverter with distributed MPPT for grid-connected applications," *IEEE Trans. Ind. Appl.*, vol. 51, no. 2, pp. 1722–1731, Mar. 2015.

[11] J. I. Y. Ota, Y. Shibano, and H. Akagi, "Low-voltage-ride-through (LVRT) capability of a phase-shifted-PWM STATCOM using the modular multilevel cascade converter based on single-star bridge-cells (MMCC-SSBC)," in *Proc. IEEE Energy Conversion Congress and Exposition*, Sep. 2013, pp. 3062–3069.

[12] J. I. Y. Ota, Y. Shibano, and H. Akagi, "A phase-shifted PWM D-STATCOM using a modular multilevel cascade converter (SSBC)-part II: Zero-voltage-ride-through capability," *IEEE Trans. Ind. Appl.*, vol. 51, no. 1, pp. 289–296, Jan. 2015.

[13] Q. Song and W. Liu, "Control of a cascade STATCOM with star configuration under unbalanced conditions," *IEEE Trans. Power Electron.*, vol. 24, no. 1, pp. 45–58, Jan. 2009.

[14] H. C. Chen, P. H. Wu, C. T. Lee, C. W. Wang, C. H. Yang, and P. T. Cheng, "Zero-sequence voltage injection for DC capacitor voltage balancing control of the star-connected cascaded H-bridge PWM converter under unbalanced grid," *IEEE Trans. Ind. Appl.*, vol. 51, no. 6, pp. 4584–4594, Nov. 2015.

[15] E. Behrouzian and M. Bongiorno, "Investigation of negative-sequence injection capability of cascaded H-bridge converters in star and delta configuration," *IEEE Trans. Power Electron.*, vol. 32, no. 2, pp. 1675–1683, Feb. 2017.

[16] Y. Yang, P. Enjeti, F. Blaabjerg, and H. Wang, "Wide-scale adoption of photovoltaic energy: Grid code modifications are explored in the distribution grid," *IEEE Ind. Appl. Mag.*, vol. 21, no. 5, pp. 21–31, Sep. 2015.

[17] H. D. Tafti, A. I. Maswood, G. Konstantinou, J. Pou, and F. Blaabjerg, "A general constant power generation algorithm for photovoltaic systems," *IEEE Trans. Power Electron.*, vol. PP, no. 99, pp. 1–1, 2017.

[18] A. Yazdani and R. Iravani, *Voltage-Sourced Converters in Power Systems:Modeling, Control, and Applications*. Wiley-IEEE Press, 2010.

[19] H. D. Tafti, A. I. Maswood, G. Konstantinou, J. Pou, K. Kandasamy, Z. Lim, and G. H. P. Ooi, "Low-voltage ride-thorough capability of photovoltaic grid-connected neutral-point-clamped inverters with active/reactive power injection," *IET Renewable Power Generation*, vol. 11, no. 8, pp. 1182–1190, Jul. 2017.

[20] F. Nejabatkhah, Y. W. Li, and B. Wu, "Control strategies of three-phase distributed generation inverters for grid unbalanced voltage compensation," *IEEE Trans. Power Electron.*, vol. 31, no. 7, pp. 5228–5241, Jul. 2016.

[21] E. Tomaszewski and J. Jiangy, "An anti-windup scheme for proportional resonant controllers with tuneable phase-shift in voltage source converters," in *proc. IEEE Power and Energy Society General Meeting (PESGM)*, Jul. 2016, pp. 1–5.

[22] R. Kabiri, D. G. Holmes, and B. P. McGrath, "Control of active and reactive power ripple to mitigate unbalanced grid voltages," *IEEE Trans. Ind. Appl.*, vol. 52, no. 2, pp. 1660–1668, Mar. 2016.

[23] R. P. Aguilera, P. Acuna, Y. Yu, G. Konstantinou, C. D. Townsend, B. Wu, and V. G. Agelidis, "Predictive control of cascaded H-bridge converters under unbalanced power generation," *IEEE Trans. Ind. Electron.*, vol. 64, no. 1, pp. 4–13, Jan. 2017.

[24] M. Mirhosseini, J. Pou, B. Karanayil, and V. G. Agelidis, "Resonant versus conventional controllers in grid-connected photovoltaic power plants under unbalanced grid voltages," *IEEE Trans. Sustainable Enery*, no. 99, pp. 1–9, Mar. 2016.

[25] D. G. Holmes and T. A. Lipo, *CarrierBased PWM of Multilevel Inverters*. Wiley-IEEE Press, 2003, pp. 453–530.

[26] Y. Li, Y. Wang, and B. Q. Li, "Generalized theory of phase-shifted carrier PWM for cascaded H-bridge converters and modular multilevel converters," *IEEE Journal of Emerging and Selected Topics in Power Electronics*, vol. 4, no. 2, pp. 589–605, Jun. 2016.

[27] H. D. Tafti, B. Vahidi, R. Naghizadeh, and S. Hosseinian, "Power quality disturbance classification using a statistical and wavelet-based hidden markov model with dempster-shafer algorithm," *Inter. Journal of Electrical Power and Energy Systems*, no. 47, pp. 368–377, Dec. 2013.

[28] M. Mirhosseini, J. Pou, V. G. Agelidis, E. Robles, and S. Ceballos, "A three-phase frequency-adaptive phase-locked loop for independent single-phase operation," *IEEE Trans. Power Electron.*, vol. 29, no. 12, pp. 6255–6259, Dec. 2014.

[29] Y. Yang and F. Blaabjerg, "Low-voltage ride-through capability of a single-stage single-phase photovoltaic system connected to the low voltage grid," *Inter. Journal of Photoenergy*, pp. 1–9, Dec. 2013.